2010 IEEE International Conference on Robotics and Automation
Anchorage Convention District
May 3-8, 2010, Anchorage, Alaska, USA

Finding Lost Wrenches: Using Continuum Robots for Contact Detection and Estimation of Contact Location

Andrea Bajo, *Student Member, IEEE,* Nabil Simaan*, *Member, IEEE*

***Abstract*—This paper presents a novel modeling framework for contact detection and estimation of contact location on multi-backbone continuum robots. The paper presents modified kinematics for constrained continuum robots and introduces the concept of Fixed Centrode Deviation (FCD) for continuum robots. It is shown that the change in fixed centrode locus may be used for detection of contact and for contact location estimation. An alternative method for contact detection using Joint Force Deviation (JFD) is investigated and a lower bound for contact detectability is derived while considering uncertainties in joint forces. An estimation framework for the location of contact is presented based on FCD and the constrained kinematics Jacobian of the continuum robot. These methods are validated by simulation and experiments. This framework may be used for enhancing the safety of robotic surgical slaves and for exploration of unknown environments such as in scenarios of search and rescue.**

I. Introduction

SUCCESFUL manipulation tasks require robots to exchange forces and moments with the environment. Force sensing is usually provided by a sensor mounted at the robot's end-effector and typically the point of contact is known *a priori*. Recently, new algorithms have been developed for sensing wrenches acting at the tip of continuum robots [1]. It was shown that continuum robots have innate sensing capabilities that make them successful robotic surgical slaves. These robots are able to estimate wrenches of interaction with the environment by monitoring their actuation forces. This capability is henceforth referred to as *intrinsic force sensing*. Among other advantages of continuum robots as surgical slaves (see [2] for details) down-scalability, MRI compatibility, and reduction of costs rely on the intrinsic force sensing capability of these robots.

Currently, the entire burden for safeguarding against damage to the anatomy is entirely placed on surgeons during telemanipulation. In an effort to enhance safety in minimally invasive surgery, robots have been limited to point interaction with anatomy and some of them (e.g. AESOP robot) use passive wrists to ensure that laparoscopic instruments satisfy the anatomic constraint of a fixed incision point [3]. Moreover, the emergence of new paradigms, such as Natural Orifice Endoscopic Trans-luminal Surgery (NOTES), requires more sophisticated surgical robots than the existing Minimal Invasive Surgery (MIS) robots. Therefore, force sensing plays a crucial role in any tele-robotic system because it reinstates the ability of the surgeon to perceive and control the interaction with the anatomy by force feedback [4-12].

In an effort to increase safety, several works focused on designing surgical tools with force sensing capabilities [13-18]. These works designed miniature force sensors placed at the distal end of the surgical devices. For example, Seibold et al. [16] developed a ∅10mm miniature 6-axis force sensor, which was mounted near the distal tip of the surgical tool. Xu [1] used continuum robots with intrinsic force sensing capability. All of these works address estimation/sensing of interaction forces at or close to the tip of surgical robots.

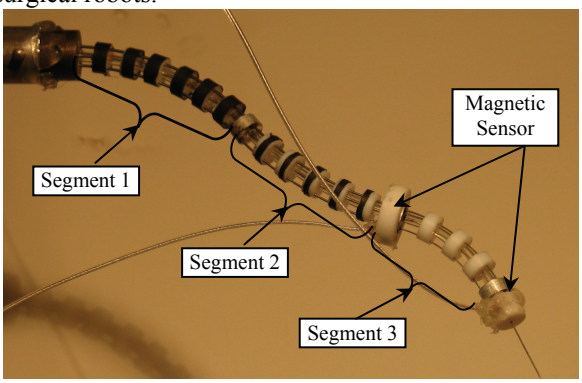

Fig. 1. A six DoF multi-backbone continuum robot composed from three segments.

Current algorithms do not address voluntary or involuntary contact of continuum robots with organs and tissues along the whole robotic structure. Sensing forces at the operational point is not enough when the workspace of the surgical robot is surrounded by delicate tissues and vital organs. Ideally, the entire robotic structure should safely move without damage to the anatomy via both auto-movements and safe interaction of any portion of the continuum robot with the anatomical environment. This basic observation motivates our investigation of new methods for contact detection along sinuous surgical slaves.

Tremendous results have been produced on force/motion control of the operational point in the last three decades [19-21]. Petrovskaya [22] used probabilistic inference and least-squares maximal likelihood approach for estimating the location of contact along a PUMA robot. The interaction forces were measured by force sensors located at two contact points. De Luca [23] presented a framework for collision detection and reaction strategies using discernable instantaneous change in the total energy and generalized

Manuscript received September 15, 2009. This work was supported by NSF Career grant #IIS-0844969. A. Bajo was partially funded by the Honors Center of Italian Universities (H2CU).

The authors are with the Department of Mechanical Engineering, Columbia University, New York, NY 10027, USA. E-mails: {ab3097, ns2236}@columbia.edu.

* Corresponding author.

momentum of the robot as a result of sudden contact. Ortmaier, [24], presented a method for kinematic estimation of the location of a trocar along a rigid robot held on an AESOP passive wrist. Dupont, [25], presented a method using hidden Markov models for estimation of kinematic constraints (contact states) during task execution. To date there are no frameworks for constraint and contact estimation for continuum robots.

The contribution of this paper is in presenting new algorithms for contact detection and estimation of location of contact for multi-backbone continuum robots. The contact may occur at any arbitrary location along the backbone of a single continuum robot, Fig. 1-(B). The methods used in this paper rely on the concept of kinematic and static deviation of the continuum robot from its unconstrained model. The concept of Fixed Centrode Deviation (FCD) is put forth to detect contact events and it is compared to another method (JFD), which relies on statics via characterization of joint force deviation. A criterion for contact detectability is presented for the JFD method and correlated with experimental results. The relevance of this contribution is for extending existing modeling frameworks for statics and kinematics of continuum multi-backbone robots [26] in order to account for estimation of contact forces, exploration of unstructured environments, and safe interaction with anatomy.

II. Kinematic Nomenclature

Fig. 1 shows a six Degree-of-Freedom (DoF) continuum multi-backbone robot. This robot is composed from three similar segments. Each segment is composed from a base disk, an end disk, spacer disks, and four super-elastic NiTi tubes. The central tube is called *primary backbone* while the other three, equally spaced apart from the primary backbone and from each other, are called *secondary backbones*. The primary backbone is attached to all the disks that compose the unit while the three secondary backbones are attached to the end disk only. Pushing and pulling two of the three secondary backbones, bends each segment in any direction in space. The redundant secondary backbone can be actuated to redistribute the actuation forces among all backbones.

Fig. 2 and Table I present the kinematic nomenclature used in the rest of this paper. The figure shows one bent segment of the continuum robot with only the primary backbone and one secondary backbone shown. An exhaustive description of the snake-like unit along with its complete and detailed kinematic and static modeling is given in [27].

Four frames are defined to facilitate the kinematic description in Fig. 2. Base frame {B} is defined with its origin at the center of the base disk and its z-axis perpendicular to the base disk. The x-axis of this frame is defined such that it passes through the location of the first secondary backbone in the base disk. Frame {1} is obtained from {B} by a simple rotation about axis $\hat{\mathbf{z}}_\mathbf{b}$ by (-δ). This frame describes the plane in which the segment bends. Frame {E} is obtained from frame {1} by a simple rotation by an angle $(\theta_0 - \theta_L)$ about $\hat{\mathbf{y}}_\mathbf{1}$. Finally, frame {G} is rigidly attached at the center of the end disk and it is obtained from {E} by a simple rotation by angle δ about axis $\hat{\mathbf{z}}_\mathbf{e}$. In addition to these frames, frame {S} is defined with its origin at arc-length *s*, its z-axis tangential to the backbone curve while its x-axis protrudes out of the $\hat{\mathbf{x}}_\mathbf{1} - \hat{\mathbf{z}}_\mathbf{1}$ plane. Note that, for $s = L$, the {S} coincides with {G}.

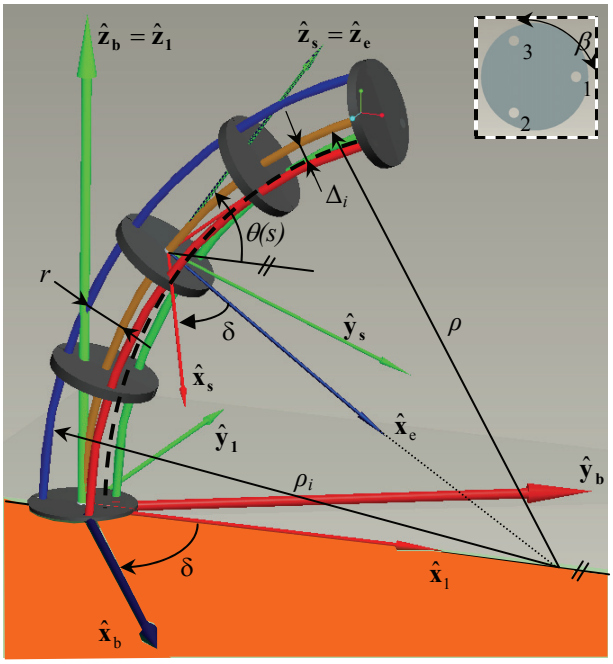

Fig. 2. Kinematic nomenclature for one-segment of the continuum robot.

TABLE I
KINEMATIC NOMENCLATURE USED IN THIS PAPER

Symbol	Description
i	index of secondary backbones, i=1,2,3
s	primary backbone arc-length parameter
L	length of the primary backbone measured from the base disk to the end disk
L_i	length of the i^{th} secondary backbone measured from the base disk to the end disk
q_i	joint parameter of the i^{th} secondary backbone. $q_i = L_i - L$
r	radius of the pitch circle defining the positions of the secondary backbones in all the disks
β	division angle of the secondary backbones along the circumference of the pitch circle. $\beta = 2\pi/3$
$\rho(s)$	radius of curvature of the primary backbone
$\rho_i(s)$	radius of curvature of the i^{th} secondary backbone
$\theta(s)$	the angle of the tangent to the primary backbone in the bending plane. We also define $\theta(0) = \theta_0 = \pi/2$, $\theta(L) = \theta_L$
δ_i	a right-handed rotation angle from $\hat{x}_1$ about $\hat{z}_1$ to a line passing through the primary backbone and the i^{th} secondary backbone at s=0
δ	$\delta \equiv \delta_1$ and $\delta_i = \delta + (i-1)\beta$
Δ_i	radial offset from the primary backbone to the projection of the i^{th} secondary backbone in the bending plane
E_P, E_S	Young's moduli of primary and secondary backbones respectively
I_P, I_S	cross-sectional moments of inertia of primary and secondary backbones respectively
E	total elastic energy of the continuum robot
ψ	configuration space vector. $\psi = [\theta_L \quad , \quad \delta]^T$

In the next section the kinematics and statics model of the continuum robot are described. Moreover, detailed position and orientation of {S} coordinate frame are given.

III. Modeling of the Continuum Robot

The instantaneous kinematics of the segment in Fig. 2 was derived in [1, 27]. In this section, we briefly review the statics of this robot and derive the kinematics Jacobian for each point along the backbone curve. In the following, the shape function, $\theta(s)$ describing the bent backbone of the segment, is assumed to be circular (this assumption was experimentally validated in [1, 28]).

The configuration of the continuum segment is parameterized by $\boldsymbol{\psi} = \begin{bmatrix}\theta_L, & \delta\end{bmatrix}^T$. The kinematic equations relating the rates of configuration variables with the twist of the end disk are:

$$\mathbf{t}_L = \mathbf{J}_{\mathbf{x}\boldsymbol{\psi}}\,\dot{\boldsymbol{\psi}} \tag{1}$$

where $\mathbf{t}_L$ designates the twist of frame {G} written using axial coordinates (linear velocity preceding the angular velocity) and the dot designates time derivative.

The joint speeds $\dot{\mathbf{q}}$ are related to the configuration variables through the following relation:

$$\dot{\mathbf{q}} = \mathbf{J}_{\mathbf{q}\boldsymbol{\psi}}\dot{\boldsymbol{\psi}}$$

$$\dot{\mathbf{q}} = \underbrace{\begin{bmatrix} r\cos(\delta) & -r(\theta_L-\theta_0)\sin(\delta) \\ r\cos(\delta+\beta) & -r(\theta_L-\theta_0)\sin(\delta+\beta) \\ r\cos(\delta+2\beta) & -r(\theta_L-\theta_0)\sin(\delta+2\beta)\end{bmatrix}}_{\mathbf{J}_{\mathbf{q}\boldsymbol{\psi}}}\dot{\boldsymbol{\psi}} \tag{2}$$

We seek a modified kinematic relation equivalent to Eq. (1), but specific to the twist of local frame {S}. This frame is given by the position $\mathbf{p}(s)$ of its origin and its orientation ${}^{\mathbf{B}}\mathbf{R}_{\mathbf{S}}$:

$$\mathbf{p}(s) = \frac{L}{(\theta_L-\theta_0)}\begin{bmatrix}\cos(\delta)\left(\sin(\theta_S)-1\right) \\ -\sin(\delta)\left(\sin(\theta_S)-1\right) \\ -\cos(\theta_s)\end{bmatrix} \tag{3}$$

$${}^{\mathbf{B}}\mathbf{R}_{\mathbf{S}}(\theta_S) = {}^{\mathbf{B}}\mathbf{R}_{\mathbf{1}}\,{}^{\mathbf{1}}\mathbf{R}_{\mathbf{E}}\,{}^{\mathbf{E}}\mathbf{R}_{\mathbf{S}} \tag{4}$$

where ${}^{\mathbf{B}}\mathbf{R}_{\mathbf{1}} = e^{-\delta[e_3\hat{}]}$, ${}^{\mathbf{1}}\mathbf{R}_{\mathbf{E}} = e^{(\theta_0-\theta_s)[e_2\hat{}]}$, and ${}^{\mathbf{E}}\mathbf{R}_{\mathbf{S}} = e^{\delta[e_3\hat{}]}$ are the exponential forms of these rotations, $\mathbf{e}_i$ designates the basis vectors for $\Re^3$, $[\mathbf{n}\hat{}]$ designates the skew-symmetric cross product matrix of vector **n,** and θ_S is a shorthand notation for $\theta(s)$. For a circular bending shape, the local tangent angle at point *s* is given by:

$$\theta_S = \pi/2 - s(\theta_0-\theta_L)/L \tag{5}$$

The corresponding twist distribution that relates the angular rate $\dot{\boldsymbol{\psi}} = \begin{bmatrix}\dot{\theta}_L & \dot{\delta}\end{bmatrix}^T$ with the angular rates $\dot{\boldsymbol{\psi}}(\mathbf{s})$ of frame {S} is given by:

$$\dot{\boldsymbol{\psi}}(\mathbf{s}) = \begin{bmatrix} s/L & 0 \\ 0 & 1\end{bmatrix}\dot{\boldsymbol{\psi}} \tag{6}$$

Using this twist distribution, the following local Jacobian is derived for frame {S}:

$$\mathbf{t}(s) = \mathbf{J}_{\mathbf{x}\boldsymbol{\psi}}(\mathbf{s})\,\dot{\boldsymbol{\psi}} \tag{7}$$

$$\mathbf{J}_{\mathbf{x}\boldsymbol{\psi}}(s, L, \theta_S, \delta) = \begin{bmatrix} \dfrac{\cos(\delta)\,\upsilon_1}{(\theta_L-\theta_0)^2} & \dfrac{L\sin(\delta)\left(1-\sin(\theta_S)\right)}{(\theta_L-\theta_0)} \\ \dfrac{\sin(\delta)\,\upsilon_1}{(\theta_L-\theta_0)^2} & \dfrac{L\cos(\delta)\left(1-\sin(\theta_S)\right)}{(\theta_L-\theta_0)} \\ \dfrac{\upsilon_2}{(\theta_L-\theta_0)^2} & 0 \\ -\sin(\delta) & \cos(\delta)\sin(\theta_S) \\ -\cos(\delta) & -\sin(\delta)\sin(\theta_S) \\ 0 & \cos(\theta_S)-1\end{bmatrix} \tag{8}$$

where $\mathbf{t}(s)$ designates the twist of the local frame {S} and variables υ_1 and υ_2 are defined as:

$$\begin{aligned}\upsilon_1 &= \sin(\theta_L-\theta_0)\cos(\theta_S) - L(\sin(\theta_S)-1) \\ \upsilon_2 &= L\cos(\theta_s) + s(\theta_L-\theta_0)\sin(\theta_s)\end{aligned} \tag{9}$$

Statics of this robot is derived using the virtual work principle [29]. Twisting, backbone extension, friction, and gravitational energy may be neglected when writing the total energy of small continuum robots

$$E = \int_L \frac{EI}{2}\left(\frac{d\theta}{ds}\right)^2 ds = (\theta_L-\theta_0)^2\left[\frac{E_P I_P}{2L} + \sum_{i=1}^{3}\frac{E_S I_S}{2L_i}\right] \tag{10}$$

An external wrench $\mathbf{W}_\mathbf{e}$ acting at the tip of the segment is related to the actuator forces $\boldsymbol{\tau}$ by this statics relation:

$$\mathbf{J}_{\mathbf{q}\boldsymbol{\psi}}{}^{\mathbf{T}}\boldsymbol{\tau} = \nabla E - \mathbf{J}_{\mathbf{x}\boldsymbol{\psi}}{}^{\mathrm{T}}\mathbf{W}_e \tag{11}$$

where ∇E is the energy gradient with respect to $\boldsymbol{\psi}$ and $\mathbf{W}_\mathbf{e}$ is the external wrench acting at the tip of the segment.

In the following section we address contact detection using the modified kinematics in Eq. (7) and the model statics in Eq. (11).

IV. Problem 1: Detection of Contact

In this section two different strategies for detection of contact are presented. The first method uses the deviation in joint forces from the nominal model given in Eq. (11) while the second method uses the modified kinematics given in Eq. (7) to detect movement of the fixed centrode. It is assumed that the continuum robot is equipped with load cells that measure the forces on the backbones and that the orientation and the position of the end disk are available through the use of a tracking device.

A. Joint Force Deviation Method

When no wrench acts on the segment, the statics of the continuum robot is given by Eq. (11) for $\mathbf{W}_\mathbf{e} = \mathbf{0}$. Once contact occurs, a deviation in the joint forces is defined as:

$$\Theta = \left\| \mathbf{J}_{\boldsymbol{\psi}\mathbf{q}}^{\mathbf{T}}\boldsymbol{\tau}_{\mathbf{lc}} - \nabla E \right\| > \xi_1 \tag{12}$$

where ξ_1 is a pre-determined threshold contact detection and $\boldsymbol{\tau}_{\mathbf{lc}}$ is the force on the backbone as measured by the load cells. If the load cells and the robot were *perfect* the

threshold ξ_1 would be zero and the system would be able to sense any contact wrench. However, in a real situation there is a lower bound for the threshold ξ_1 below which no contact is detectable. If friction forces $\boldsymbol{\tau}_\mathbf{f}$ exist in the mechanical transmission lines, the load cell forces $\boldsymbol{\tau}_\mathbf{lc}$ are related to the backbone forces according to:

$$\boldsymbol{\tau} = \boldsymbol{\tau}_\mathbf{lc} - \boldsymbol{\tau}_\mathbf{f} = (1-\varepsilon_\tau)\boldsymbol{\tau}_\mathbf{lc} \tag{13}$$

where ε_τ designates the relative error in the load cell measurements such that $\boldsymbol{\tau}_\mathbf{f} = \varepsilon_\tau \boldsymbol{\tau}_\mathbf{lc}$. Eq. (11) can now be rewritten as

$$\mathbf{J}_{\mathbf{q}\psi}{}^{\mathbf{T}}(1-\varepsilon_\tau)\boldsymbol{\tau}_{\mathrm{lc}} - \nabla \mathrm{E} = \mathbf{0} \tag{14}$$

Considering these errors, one may now define the deviation in the joint forces as

$$\varepsilon_c = \sqrt{\left(\mathbf{J}_{\mathbf{q}\psi}^{\mathbf{T}}(1-\varepsilon_\tau)\boldsymbol{\tau}_\mathbf{lc} - \nabla \mathbf{E}\right)^{\mathrm{T}}\left(\mathbf{J}_{\mathbf{q}\psi}^{\mathbf{T}}(1-\varepsilon_\tau)\boldsymbol{\tau}_\mathbf{lc} - \nabla \mathbf{E}\right)} \tag{15}$$

Since we lumped all uncertainties in $\boldsymbol{\tau}_\mathrm{f}$, $\mathbf{J}_{\mathbf{q}\psi}^{\mathbf{T}}\boldsymbol{\tau}_\mathbf{lc} - \nabla \mathbf{E} = \mathbf{0}$ (i.e., outside the effects of $\boldsymbol{\tau}_\mathrm{f}$ the robot and load cells are perfect) so Eq. (15) simplifies to:

$$\varepsilon_c = \varepsilon_\tau \sqrt{\boldsymbol{\tau}_\mathbf{lc}{}^{\mathbf{T}}\mathbf{J}_{\mathbf{q}\psi}\mathbf{J}_{\mathbf{q}\psi}^{\mathbf{T}}\boldsymbol{\tau}_\mathbf{lc}} \tag{16}$$

For a given estimate of the friction, one may compute ε_τ and calculate ε_c, which is the lower bound for contact detectability threshold ξ_1. If $\xi_1 < \varepsilon_c$ contact will be falsely detected due to friction and load cell errors. Fig. **3** shows a plot of ε_c versus the bending angle θ_L for different values of ε_τ. From the graph it is found that when the snake is fully straight the effects of friction become attenuated. This observation also agrees with our discussion in [1] regarding the superior wrench estimation accuracy of these robots.

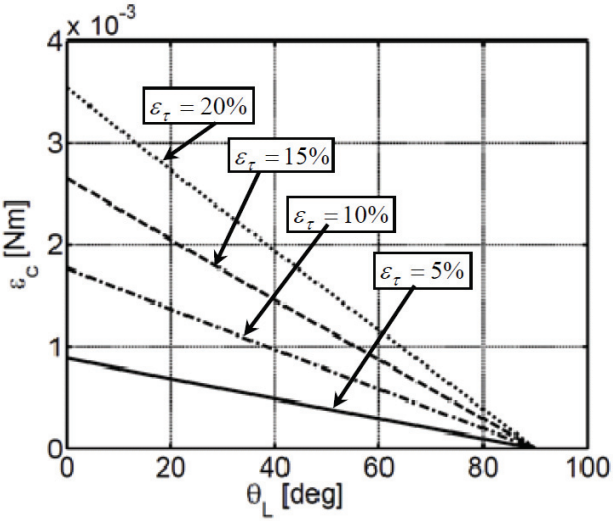

Fig. 3. Theoretical contact detectability lower thresholds for JFD method for different values of relative load cell error $\boldsymbol{\varepsilon}_\boldsymbol{\tau}$.

B. Fixed Centrode Deviation Method

The previous method relies on statics and provides a method for contact detectability even when the snake is at rest. However, the method does not provide the location of the contact. The FCD method is based on the deviation between the actual and the theoretical loci of the fixed centrode of the end disk when in motion. Let $\mathbf{c}_\mathbf{m}$ be the location of the instantaneous screw axis of the end disk

$$\mathbf{c}_\mathbf{m} = \frac{\boldsymbol{\Omega}_\mathbf{m}(\dot{\mathbf{p}}_\mathbf{m} - \boldsymbol{\Omega}_\mathbf{m}\mathbf{p}_\mathbf{m})}{\boldsymbol{\omega}_\mathbf{m}{}^{\mathbf{T}}\boldsymbol{\omega}_\mathbf{m}} \tag{17}$$

where $\dot{\mathbf{p}}_\mathbf{m}$ and $\boldsymbol{\omega}_\mathbf{m}$ are the linear and angular velocity components of the end disk twist as predicted by the kinematic model in Eqs. (1), (2), and (8) calculated for $\mathrm{s} = \mathrm{L}$ and $\boldsymbol{\Omega}_\mathbf{m} = [\boldsymbol{\omega}_m]^\wedge$ is the skew-symmetric angular-velocity matrix.

Let us now assume that the end disk is tracked by a sensor capable of providing position and orientation. The pose of the end disk is described by

$$\mathrm{x}_\mathrm{s} = \begin{bmatrix}\mathrm{p_x} & \mathrm{p_y} & \mathrm{p_z} & \alpha & \gamma & \lambda\end{bmatrix}^{\mathrm{T}}$$

where $\mathrm{p_x}$, $\mathrm{p_y}$, and $\mathrm{p_z}$ are the *x*, *y*, and *z* coordinates of the position of the end disk, and α, γ, and λ are Euler's angles describing its orientation. The location of the instantaneous screw axis according to the sensor's data is given by

$$\mathbf{c}_\mathbf{s} = \frac{\boldsymbol{\Omega}_\mathbf{s}(\dot{\mathbf{p}}_\mathbf{s} - \boldsymbol{\Omega}_\mathbf{s}\mathbf{p}_\mathbf{s})}{\boldsymbol{\omega}_\mathbf{s}{}^{\mathbf{T}}\boldsymbol{\omega}_\mathbf{s}} \tag{18}$$

where $\boldsymbol{\Omega}_\mathbf{s} = \dot{\mathbf{R}}_\mathbf{s}\mathbf{R}_\mathbf{s}^{\mathbf{T}}$ and $\boldsymbol{\omega}_\mathbf{s} = [\boldsymbol{\Omega}_\mathbf{s}]^\vee$ are the angular-velocity matrix and the angular velocity vector as obtained from the sensor orientation $\mathbf{R}_s$. The sensor orientation matrix is defined as:

$$\mathbf{R}_\mathbf{s} = \mathbf{R}(\alpha,\gamma,\lambda)\tilde{\mathbf{R}}_\mathbf{g}$$

where $\mathbf{R}(\alpha,\gamma,\lambda)$ is the time variant rotation matrix associated with the chosen Euler's angles representation and $\tilde{\mathbf{R}}_\mathbf{g}$ is a constant rotation matrix that describes the orientation of {G} with respect to a frame attached to the sensor's marker.

Collision is, therefore, detected when

$$\left\|\mathbf{c}_\mathrm{m} - \mathbf{c}_\mathrm{s}\right\| > \xi_2 \tag{19}$$

where ξ_2 is a threshold for contact detectability.

V. Problem 2: Estimation of Contact Location

In this section, a constrained kinematic model of the robot is introduced to estimate the location of contact. Assume that the contact acts at an unknown location $\mathrm{s} = \mathrm{s_c}$ along the primary backbone. Fig. 4(b) shows the kinematic behavior of the continuum robot when one of the middle disks is constrained. The lower part of the snake-like unit remains almost fixed while the top part continues bending. Both parts maintain a quasi-circular shape that allows one to use the simplified kinematic model presented in section III. The unconstrained part of the snake-like unit behaves like a shorter segment of length $\mathrm{L} - \mathrm{s_c}$. The constrained disk becomes the base disk of the unconstrained portion of the unit. Using Eq. (1) we describe the twist of the end disk by $\tilde{\mathbf{t}}$ (given with respect to stationary frame {S}):

$$\tilde{\mathbf{t}} = \tilde{\mathbf{J}}_{\mathbf{x}\psi}\,\dot{\tilde{\boldsymbol{\psi}}} \tag{20}$$

where $\tilde{\mathbf{J}}_{\mathbf{x}\psi}$ is the Jacobian of the unconstrained portion as

given by substituting the input arguments $\tilde{L} = L - s_c$, $s = \tilde{L}$, $\tilde{\theta}_s = \theta_0 + \theta_L - \theta(s_c)$, $\tilde{\delta} = \delta$ into Eq. (8). Since the constrained segment of the snake is stationary, the configuration space velocities of the unconstrained portion are given by $\dot{\tilde{\psi}} = \dot{\psi}$.

The constrained twist $\mathbf{t}_c$ of the end disk can be transformed from local frame {S} to {B} as

$$\mathbf{t}_c = {}^{B}\mathbf{T}_S \tilde{\mathbf{t}} = {}^{B}\mathbf{T}_S \tilde{\mathbf{J}}_{x\psi} \dot{\tilde{\psi}} = \bar{\mathbf{J}}_{x\psi} \dot{\psi} \tag{21}$$

where $\bar{\mathbf{J}}_{x\psi}$ is called the *constrained Jacobian* and ${}^{B}\mathbf{T}_S$ is a 6×6 block-diagonal matrix defined as:

$${}^{B}\mathbf{T}_S = \begin{bmatrix} {}^{B}\mathbf{R}_S & \mathbf{0} \\ \mathbf{0} & {}^{B}\mathbf{R}_S \end{bmatrix} \tag{22}$$

In Eq. (22), ${}^{B}\mathbf{R}_S$ is obtained by substituting $\theta_s = \theta_{s_c}$ in Eq. (4) where θ_{s_c} is the angle of the end disk of the constrained segment as obtained from Eq. (5) substituting $s = s_c$ at the instant when contact is first detected.

Using Eq. (22), the location of the instantaneous screw axis of the constrained end disk in {B} is given by

$$\mathbf{c}_c(s_c) = \frac{\boldsymbol{\Omega}_c(\dot{\mathbf{p}}_c - \boldsymbol{\Omega}_c \mathbf{p}_c)}{\boldsymbol{\omega}_c^{T} \boldsymbol{\omega}_c} \tag{23}$$

where $\boldsymbol{\Omega}_c = [\boldsymbol{\omega}_c]^{\wedge}$, $\mathbf{p}_c = \mathbf{p}(\mathbf{s}_c) + {}^{B}\mathbf{R}_S \tilde{\mathbf{p}}_c$, and $\tilde{\mathbf{p}}_c$ indicates the position of the end disk in {S}.

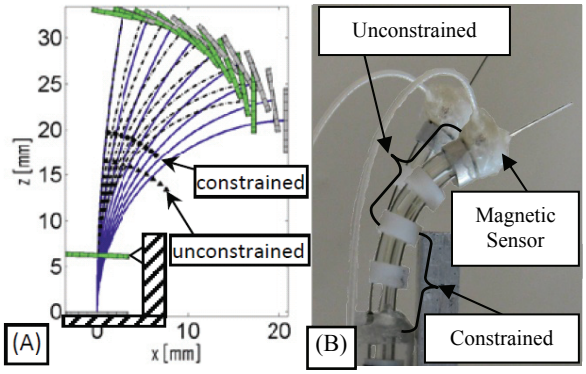

Fig. 4. Constrained and unconstrained motion of one segment. (A) Fixed centrode loci with or without constraint. (B) Image overlay of constrained segment. The contact happens at the second disk.

Fig. 4 shows the change of the fixed centrode loci when one of the middle disks of the continuum segment is constrained. The solid lines sketch the motion of the primary backbone of the unconstrained continuum robot while the dashed lines indicate the motion of the primary backbone of the constrained robot. The fixed centrode locus of the constrained unit (circles) moves along a different curve from the fixed centrode locus of the unconstrained segment (triangles).

The location of contact s_c is found by the value of s that minimizes the Euclidian distance between the locus of the fixed centrode $\mathbf{c}_s$ as obtained from the sensor and the locus of the constrained fixed centrode $\mathbf{c}_c$, that is:

$$s_c = \arg\min_s \left(\left\| \mathbf{c}_c(\mathbf{s}) - \mathbf{c}_s \right\| \right) \tag{24}$$

VI. Experimental Evaluation

This section presents the experimental setup, the set of experiments that have been conducted, and experimental results testing the efficacy of the JFD and FCD methods for contact detection and estimation of location of contact. The experimental setup shown in Fig. 5 includes the three segment continuum robot and two types of sensors: load cells for monitoring the actuation forces and a magnetic tracker that tracks the pose of the end disk of the robot. In all experiments we have constrained the first two segments and used only the last segment. An Ascension 3D Guidance trackSTAR magnetic tracker with a static resolution of 0.5 mm in position and 0.1° in orientation was used. The actuation unit of the continuum robot was controlled using Matlab xPC Target real time operating system with 1 KHz of position control frequency. The magnetic tracker was sampled at the same frequency, though its refresh rate from the tracker unit was 100 Hz. Communication between the magnetic tracker and the target machine was achieved using UDP. In the following subsections three different experiments are presented: detection of the contact event using the concept of JFD, detection of the contact event using the concept of FCD, and estimation of contact location.

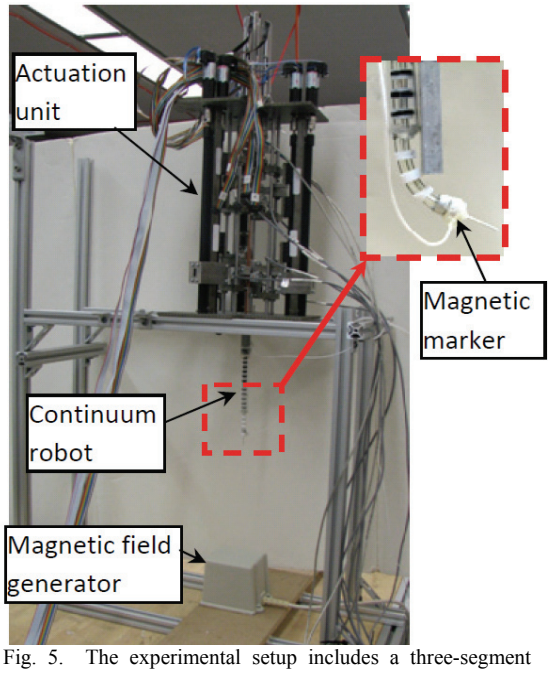

Fig. 5. The experimental setup includes a three-segment continuum robot (only one segment is actuated), actuation units with load cells, and a magnetic tracker device.

A. Detection of contact via JFD

The strategy based on the concept of JFD naturally follows from the statics of the continuum robot and it was the first one to be investigated. However, since our robot is not calibrated and its internal friction is not characterized, we observed non-constant error in the statics model when the unconstrained robot scanned its workspace. To test the

feasibility of this method, we conducted experiments and calculated Θ (Eq. 12) for the same segment when moved with and without constraint. The segment was bent from a straight configuration by 60º and the actuation forces were recorded together with the position and orientation of the end disk. The contact point for the constrained case was tested at many points along the backbone. Fig. 6 shows a characteristic result for a contact point present at the middle of the segment. The experiments were repeated five times for both the constrained and unconstrained case in order to test the repeatability of our results. It was found that contact is marked by a distinguishable deviation between the curves of Θ for the constrained and unconstrained case. In Fig. 6 the contact occurred at 6.5 seconds.

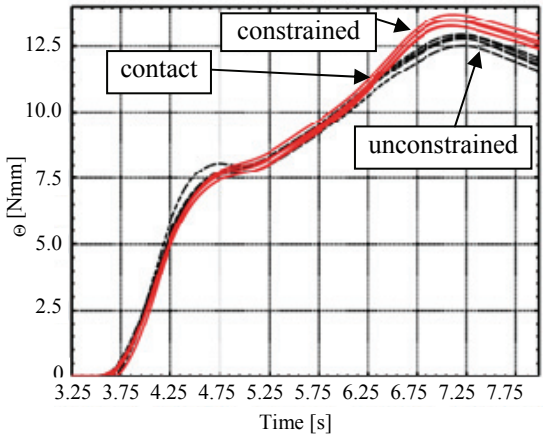

Fig. 6. Experimental results showing contact detection for the un-calibrated continuum segment of Fig. 4. Detection of contact is achieved by the deviation in the value of Θ (Eq. 12). The contact point was located at mid-length of the segment.

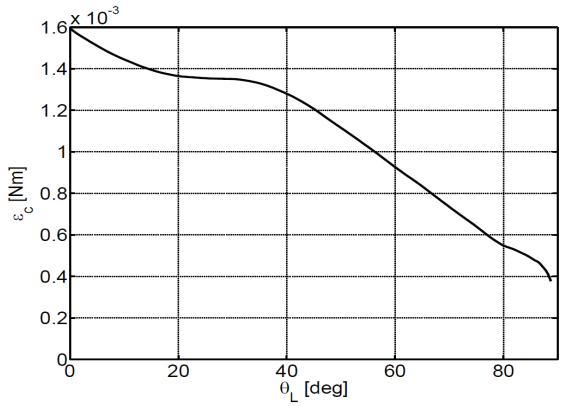

Fig. 7. The value of ε_c for our un-calibrated continuum segment

Our experience using this method indicates that it depends strongly on calibration of friction and calibration of the actuator forces for an unloaded snake. Noise in the load cells reading and the difficulty in determining a suitable ε_c stem from the fact that calibration is needed and that the threshold is not necessarily constant as seen in Fig. 3.

During the experiment, the snake segment is bent from the initial configuration θ_L=90° to θ_L=30° and the residual Θ at each time step was recorded. Fig. 7 shows that the residual Θ is not constant when the snake-like unit bends. This result agrees with our simulations in Fig. 3. Comparison of the results in Fig. 7 and Fig. 3 show that we are able to estimate the percentage of load cell/friction/model calibration uncertainty at 10%. After calibration, it would be possible to tune a threshold and detect the collision using a pre-set threshold. This technique is a valid alternative to FCD method when the robot is at rest. In fact, the FCD is not defined when the angular velocity of the end disk is zero.

B. *Detection of contact via FCD*

The strategy based on the concept of FCD allows one to define a constant threshold along the workspace of the robot because the deviation of the actual kinematics from the *ideal* kinematics of the continuum robot is relatively small. The segment was bent in several experiments from θ_L=90° to θ_L=0° and a contact constraint was placed along several known points along the backbone. For each fixed contact point, the experiment was repeated at least five times to verify repeatability of our results.

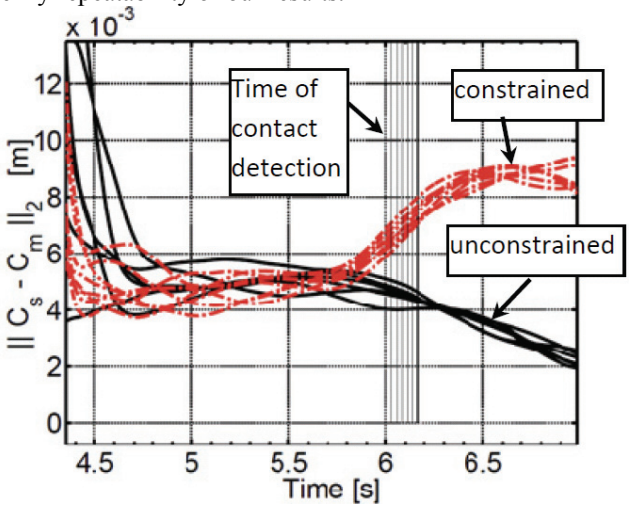

Fig. 8. Contact detection using the FCD method. The experiment has been conducted multiple times to test the repeatability of the detection. Contact occurs between 6 and 6.2 seconds.

Fig. 8 shows typical experimental data demonstrating contact detection. The vertical dashed lines indicate the detection of contact in several repetitions of experiments. Because of the trajectory profile (a 5th order rest-to-rest polynomial with execution time of 5 seconds and t_{start}=3s, t_{final}=8s), the computation of the centrode of motion in the first few seconds has an abrupt transient. In particular, the instability is due to the very low angular velocity of the robot end disk when the segment is fully straight (θ_L=90°) and because of filtering of the tracker readings that it is indispensable for obtaining a smooth reading from the magnetic tracker. A moving average filter with 500 samples and a sample time of 0.001s was used for tracker readings. Despite these difficulties, the figure shows that the error stabilizes after t=5s. The contact detection algorithm is, therefore, activated after t=5s. Several collisions with a static constraint beam (Fig. 4-(B)) have been detected between t=6.02s and t=6.16s. These results show high repeatability of the collision detection. Furthermore, the threshold for contact used in the experiments has been determined empirically and without any fine tuning. Clearly, the figure

shows that the dash-point curves deviate from the group of curves earlier than t=6.02s. The threshold used for the centrode deviation was 0.007 [m].

C. Estimation of location of contact

This last subsection presents results of the estimation of location of contact algorithm (ELC). This algorithm was implemented in real-time as well as the previous one. Once the previous algorithm detects a collision, a snapshot of the system is taken. Hence, the instant of time t_c, the configuration of the robot $\boldsymbol{\psi}_c$, and the current centrode $\mathbf{c_s}$ based on (18) are fed into the ELC algorithm. The algorithm uses the information on the instant of contact t_c to compute the desired $\dot{\boldsymbol{\psi}}(t_c)$, and then uses Eq. (23) and Eq. (24) to estimate the location of contact. Since the segment is relatively small, the algorithm tests a discrete set of point along the interval $s \in (0, L)$ and returns the one that minimizes Eq. (24).

TABLE II
EXPERIMENTAL RESULTS FOR DIFFERENT LOCATIONS ALONG THE BACKBONE OF THE CONTINUUM ROBOT

Disk	Time of Contact [s]	Bending angle at contact θ_L [rad]	Estimated location of contact s_c [m]	Standard deviation of s_c σ [m]
1	7.1340	0.1190	0.0060	
1	7.1560	0.1126	0.0050	
1	5.7640	0.8067	0.0090	0.0017
1	7.2680	0.0745	0.0050	
1	7.1670	0.1078	0.0050	
2	6.2870	0.7181	0.0160	
2	6.2910	0.7246	0.0160	
2	6.2970	0.7204	0.0170	7.0711×10^{-4}
2	6.2580	0.7392	0.0150	
2	6.2710	0.7277	0.0160	
3	5.6420	1.0563	0.0080	
3	5.6380	1.0616	0.0080	
3	5.6340	1.0575	0.0090	0.0012
3	5.6580	1.0481	0.0110	
3	5.6140	1.0674	0.0090	

Table II shows the experimental results conducted with different location of contact along the segment of the continuum robot. The first column of this table indicates which of the disks was in contact with the environment. The length of the primary backbone was 30 mm and the middle disks are placed at 7.5 mm (Disk 1), 15mm (Disk 2), and 22.5 mm (Disk 3) with respect to the base disk. The snake-like unit bends from θ_L=90° to θ_L=0° in 5 seconds following a 5th order polynomial rest-to-rest profile. The second column shows the bending angle at which the contact is detected. The third column reports the estimated location of the contact along the backbone curve, and the fourth column shows the standard deviation of the estimated location of contact within the group of five experiment repetitions.

From the results, it is evident that a contact closer to the tip of the unit allows faster collision detection. However, this configuration also leads to a poorer estimation of location of contact. The poor estimate is due to the near buckling of the unit and in turn invalidation of the assumption of a small change to the shape of the constrained section.

Excellent results are obtained when the contact occurs at the middle disk. The bending angle at detection is 42° and the standard deviation σ associated with this set of experiments is small. Good results are also obtained when the contact happens at the first disk. Because of the fact that, when the continuum robot bends, the first disk does not move significantly until a very small bending values of θ_L are reached, meaning large bending angles, requiring a longer time for contact detection. In fact, the actual deviation of the twist from the ideal one is small for most part of the movement.

Results show the effectiveness of the estimation of the contact location. Prediction errors and false positives are due to several issues (not addressed in this paper) such as: kinematic calibration of the robot, use of the simplified circular bending shape instead of the exact shape, limitations due to the sensors (resolution of the magnetic tracker) and the relatively small length of the snake-like unit.

VII. CONCLUSIONS

Despite the many works on force control and contact detection, continuum robots lack a framework for contact detection and estimation of location of unknown wrenches. This paper presented two methods for contact detection and estimation of location of an unknown contact wrench along the backbone of multi-backbone robots. It is assumed that two types of sensors are available for detecting contact. The first type of sensors is load cells used for measurement of joint forces. The second type of sensors provide position and orientation information used to calculate the instantaneous pose of the end-effector. The constrained kinematics of single-segment continuum robot was derived and used for two methods of contact detection. While the first method (JFD) relies on statics and works in scenarios where no movement is necessary to discern contact, the second method (FCD) relies on kinematics and requires movement. Lower bounds for contact detectability based on estimates of joint force errors were obtained.

It was shown that the method of fixed centrode deviation is quite repeatable for contact detection while the joint force deviation was more difficult to use due to difficulties in calibrating the continuum robot.

The ability for contact detection and estimation of location of contact provides a possibility for estimating wrenches of contact and segmenting different constraint scenarios that are relevant for exploration of unstructured environments and necessary for the next generation of medical robots that are required to interact safely with the anatomy and reach deep into the human body.

Future work will focus on estimation of multiple contacts acting on continuum robots and design of control algorithms that rely on these new capabilities for exploration of rigid unstructured environments.

REFERENCES

[1] K. Xu and N. Simaan, "An Investigation of the Intrinsic Force Sensing Capabilities of Continuum Robots", in *IEEE Transactions on Robotics*, Vol. 24, NO. 3, pp. 576-586, June 2008.

[2] N. Simaan, K. Xu, W. Wei, A. Kapoor, P. Kazanzides, R. Taylor, and P. Flint, "Design and Integration of a Telerobotic System for Minimally Invasive Surgery of the Throat", in *The International Journal of Robotics Research,* Vol. 28, pp. 1134-1153, May 2009.

[3] R. Taylor and D. Stoianovici, "Medical Robotics in Computer-Integrated Surgery", in *IEEE Transactions on Robotics and Automation*, Vol. 19, NO. 5, pp. 765-781, October 2003.

[4] L. N. Verner and A. M. Okamura, ″Sensor/Actuator Asymmetries in Telemanipulators: Implications of Partial Force Feedback", in *Symposium on Haptic Interfaces for Virtual Environment and Teleoperator Systems* 2006, Alexandria, Virginia, USA.

[5] M. C. Çavuşoğlu, A. Sherman, and F. Tendick, "Design of Bilateral Teleoperation Controllers for Haptic Exploration and Telemanipulation of Soft Environments" in *IEEE Transactions on Robotics and Automation*, Vol. 18. NO. 4, pp.641-647, August 2002.

[6] F. Tendick, M.C. Çavuşoğlu, N. Dhruv, and A. Sherman, "Maximizing the Sensation of Compliance in Teleoperative Surgery" in *Proc. of the Eighth International Symposium on Robotics with Applications,* June 11-16, 2000, Maui, HI.

[7] C. Wagner, N. Stylopoulos, and R. Howe, "The Role of Force Feedback in Surgery: Analysis of Blunt Dissection", in *Proc. of the Tenth Symposium on Haptic Interfaces for Virtual Environment and Teleoperator Systems*, March 24-25, 2002, Orlando, USA.

[8] M. Mahvash and A. M. Okamura, "Friction Compensation for a Force-Feedback Telerobotic System", in *Proc. of the 2006 IEEE International Conference on Robotics and Automation,* Orlando, Florida, May 2006.

[9] A. M. Okamura, "Methods for Haptic Feedback in Teleoperated Robot-Assisted Surgery", in *International Journal of Industrial Robot*, Vol. 31, pp. 499-508, 2006.

[10] C. R. Wagner, D. P. Perrin, R. D. Howe, N. Vasilyev, P. J. Del Nido, "Force feedback in a three-dimensional ultrasound-guided surgical task" in *Proc. of the Symposium on Haptic Interfaces for Virtual Environment and Teleoperator System 2006,* Alexandria, VA, March 25 - 29, 2006.

[11] G. Tholey, J.P. Desai, and A. E. Castellanos, "Evaluating the role of vision and force feedback in minimally invasive surgery: New automated laparoscopic grasper and a case study", in 2003 *Medical Image Computing and Computer-Assisted Intervention,* Montreal, Quebec, Canada, 2003.

[12] K. J. Kuchenbecker, N. Gurari, and A.M. Okamura, ″Quantifying the value of visual and haptic position feedback during force-based motion control", in *Second Joint EuroHaptics Conference and Symposium on Haptic Interfaces for Virtual Environment and Teleoperator Sustems (WHC'07)*, Tsukuba, Japan, 2007.

[13] K. Ikuta, S. Daifu, T. Hasegawa, and H. Higashikawa, "Hyper-finger for Remote Minimally Invasive Surgery in Deep Area", in *Medical Image Computing and Computer-Assisted Intervention - MICCAI*, Tokyo, Japan, 2002.

[14] M. Tavakoli, R.V. Patel, and M. Moallem, "A Force Reflective Master-Slave System for Minimally Invasive Surgery", in *Proc. of the 2003 IEEE/RSJ International Conference on Intelligent Robots and Systems*, Las Vegas, Nevada, October 2003.

[15] S. Shimachi, Y. Fujiwara, and Y. Hakozaki, "New Sensing Method of Force Acting on Instrument for Laparoscopic Robot Surgery", in *Proc. of the Computer Assisted Radiology and Surgery - CARS,* 2004.

[16] U. Seibold, B. Kübler, and G. Hirzinger, "Prototype of Instrument for Minimally Invasive Surgery with 6-Axis Force Sensing Capability", in *Proc. of the 2005 IEEE International Conference on Robotics and Automation,* Barcelona, Spain, April 2005.

[17] K. Tadano and K. Kawashima, "Development of 4-DoFs Forceps with Force Sensing using Pneumatic Servo System", in *Proc. of the 2006 IEEE International Conference on Robotics and Automation,* Orlando, Florida, May 2006.

[18] M. Mitsuishi, N. Sugita, and P. Pitakwatchara, "Force-Feedback Augmentation Modes in the Laparoscopic Minimal Invasive Telesurgical System", in *IEEE/ASME Transaction on Mechatronics*, Vol. 12, NO. 4, pp. 447-454, August 2007.

[19] B. Siciliano, L. Villani, "Robot Force Control", *Kluwer Academic Publishers*, 1999.

[20] B. L. Davies, K. L. Fan, R. D. Hibberd, M. Jakopec, S. J. Harris, *ACROBOT - Using Robots and Surgeons Synergistically in Knee Surgery*, in *Proc. of the 1997 International Conference on Advanced Robotics,* Monterey, CA, Julay 7-9, 1997.

[21] J. Park and O. Khatib, "Robot Multiple Contact Control", in *Robotica*, Vol. 26, Issue 4, pp. 667-677, September 2008.

[22] A. Petrovskaya, J. Park, and O. Khatib, "Probabilistic Estimation of Whole Body Contacts for Multi-Contact Robot Control", in *Proc. of the 2007 IEEE International Conference on Robotics and Automation*, Roma, Italy, 10-14 April, 2007.

[23] A. De Luca, A. Albu-Schäffer, S. Haddin, G. Hirzinger, "Collision Detection and Safe Reaction with the DLR-III Lightweight Manipulator Arm", in *Proc. of the 2006 IEEE/RSJ International Conference on Intelligent Robots and Systems,* Beijin, China, 9-15 October, 2006.

[24] T. Ortmaier and G. Hirzinger, "Cartesian Control Issues for Minimally Invasive Robot Surgery", in *Proc. of the 2000 IEEE/RSJ International Conference on Intelligent Robots and Systems,* 2000.

[25] T. Debus, P. Dupont, and R.D. Howe, "Contact state estimation using multiple model estimation and hidden Markov models", in *Experimental Robotics VIII,* Vol. 5, 2003.

[26] D. B. Camarillo, C. F. Milne, C. R. Carlson, M. R. Zinn, and J. K. Salisbury, "Mechanics modeling of tendon-driven continuum manipulators", in *IEEE Transactions on Robotics*, Vol. 24, NO. 6, pp. 1262-1273, December 2008.

[27] N. Simaan, R. Taylor, and P. Flint, "A Dexterous System for Laryngeal Surgery - Multi-Backbone Bending Snake-like Slaves for Teleoperated Dexterous Surgical Tool Manipulation", in *Proc. of the 2004 IEEE International Conference on Robotics and Automation,* New Orleans, LA, April 2004.

[28] I. Gravagne and I. D. Walker, "Kinematic Transformations for Remotely-Actuated Planar Continuum Robots", in *Proc. of the 2000 IEEE International Conference on Robotics and Automation*, San Francisco, CA, April 2000.

[29] N. Simaan, "Snake-Like Units Using Flexible Backbones and Actuation Redundancy for Enhanced Miniaturization", in *Proc. of the 2005 IEEE International Conference on Robotics and Automation,* Barcelona, Spain, April 2005.

[30] B. S. Eberman and J. K. Salisbury, "Determination of manipulator contact information from joint torque measurements", in *Experimental Robotics I,* Vol. 139, pp 463-473, 1990.